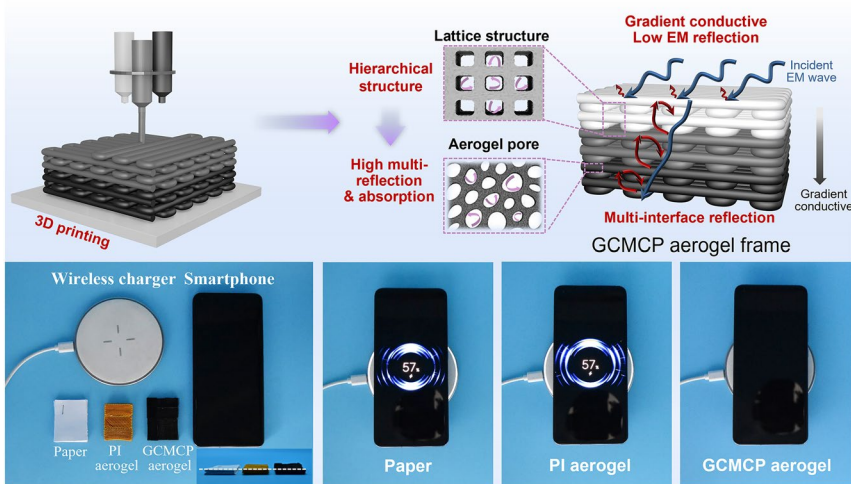# 3D Printed Integrated Gradient-Conductive MXene/CNT/Polyimide Aerogel Frames for Electromagnetic Interference Shielding with Ultra-Low Reflection

Tiantian Xue[1], Yi Yang[1], Dingyi Yu[1], Qamar Wali[4], Zhenyu Wang[3], Xuesong Cao[3], Wei Fan[1,2] ✉, Tianxi Liu[1,2] ✉

HIGHLIGHTS

- The MXene/CNT/Polyimide aerogel frame with integrated gradient-conductive structure was constructed by MXene/CNT/poly(amic acid) composite inks with different CNT contents via 3D printing technology.

- The integrated gradient-conductivity and hierarchical porous structure of MXene/CNT/Polyimide aerogel frame rendered excellent electromagnetic interference shielding performance and ultra low reflection.

ABSTRACT Construction of advanced electromagnetic interference (EMI) shielding materials with miniaturized, programmable structure and low reflection are promising but challenging. Herein, an integrated transition-metal carbides/carbon nanotube/polyimide (gradient-conductive MXene/CNT/PI, GCMCP) aerogel frame with hierarchical porous structure and gradient-conductivity has been constructed to achieve EMI shielding with ultra-low reflection. The gradient-conductive structures are obtained by continuous 3D printing of MXene/CNT/poly (amic acid) inks with different CNT contents, where the slightly conductive top layer serves as EM absorption

layer and the highly conductive bottom layer as reflection layer. In addition, the hierarchical porous structure could extend the EM dissipation path and dissipate EM by multiple reflections. Consequently, the GCMCP aerogel frames exhibit an excellent average EMI shielding efficiency (68.2 dB) and low reflection ($R = 0.23$). Furthermore, the GCMCP aerogel frames with miniaturized and programmable structures can be used as EMI shielding gaskets and effectively block wireless power transmission, which shows a prosperous application prospect in defense industry and aerospace.

KEYWORDS 3D printing; MXene/CNT/Polyimide aerogel; Gradient-conductive; Electromagnetic interference shielding

✉ Wei Fan, weifan@dhu.edu.cn; Tianxi Liu, txliu@jiangnan.edu.cn

1 State Key Laboratory for Modification of Chemical Fibers and Polymer Materials, College of Materials Science and Engineering, Donghua University, 2999 North Renmin Road, Shanghai 201620, People's Republic of China

2 Key Laboratory of Synthetic and Biological Colloids, Ministry of Education, School of Chemical and Material Engineering, Jiangnan University, Wuxi 214122, People's Republic of China

3 Institute of Environmental Processes and Pollution Control, School of Environment and Civil Engineering, Jiangnan University, Wuxi 214122, People's Republic of China

4 NUTECH School of Applied Sciences & Humanities, National University of Technology, Islamabad 44000, Pakistan

1 Introduction

With the prosperity of microelectronics and 5th generation mobile communication technology, it is necessary to develop lightweight, programmable structure and ultra-efficient electromagnetic interference (EMI) shielding materials to ensure proper operation of electronic devices and human health [1–3]. Currently, polymer-based conductive composites are rapidly developed as EMI shielding materials benefiting to their corrosion resistance, easy processing and flexible design of conductive networks [4–6]. However, polymer-based EMI shielding materials with a homogeneous high conductive network exhibit high reflection of electromagnetic waves into free space, leading to serious secondary electromagnetic radiation contamination [7–9]. To minimize the secondary electromagnetic radiation pollution, absorption-dominated EMI shielding polymer composites with low reflection are greatly desired for next-generation electronic devices. Yet, polymer-based EMI shielding materials with low conductivity would effectively reduce the reflection of electromagnetic waves, but inevitably reduces the EMI shielding efficiency (EMI SE) due to weak absorption losses within the material [10, 11]. Therefore, an improved understanding between structure and functionality of polymer-based EMI shielding material is critical for design and development of advanced EMI shielding materials with low reflection and high absorption.

In recent years, lightweight aerogels with high porosity are considered as promising materials for EMI shielding [4, 12]. Benefit to the three-dimensional (3D) porous structure of aerogel, the incident electromagnetic waves can be multiple reflected/scattered and lost in the porous structure, thus enhancing the EMI shielding performance, especially its electromagnetic wave absorption ability [13, 14]. For instance, Zhao et al. [15] reported transition-metal carbides (MXenes)/graphene oxide (GO) hybrid aerogel with aligned cellular microstructure and high conductivity (1085 S m^{-1}), which effectively performs electron transfer and microwave attenuation exhibiting high EMI shielding effectiveness (EMI SE = 50 dB in the X band). In addition, Zeng et al. [16] prepared silver nanowire/cellulose composite aerogels with laminar, honeycomb and random porous structures by adjusting the freezing method, where the laminar-structured aerogels have high EMI shielding properties and low density. However, this uniform conductive network of aerogels

leads to an impedance mismatch between the air-material interface, causing electromagnetic waves to be reflected into free space and forming secondary electromagnetic radiation pollution. Therefore, Xu et al. [17] constructed a gradient-conductive structure via sedimentation of the conductive filler with different densities, which can absorb-reflect-reabsorb electromagnetic wave, showing an excellent EMI SE value of nearly 87.2 dB and a reflection coefficient (R) of 0.39. Hu et al. [18] constructed a low-conductive impedance matching layer on top of the highly conductive material by a layer-by-layer method, thus reducing the reflection of electromagnetic waves and obtaining low SE_R of 0.29 dB. Therefore, constructing a porous structure as well as reasonable gradient-conductive structure is a feasible way to effectively enhance the EMI SE and reduce reflection coefficient [19–21]. However, due to the cumbersome and unreliable construction of gradient-conductive structures via sedimentation or layer-by-layer methods, it is still a challenge to fabricate absorption-dominated polymer-based EMI shielding materials with low reflection coefficient.

3D printing technology is a promising technology with the advantages of complex structure formation and multi-component integration [22–27]. The integrated construction of gradient-conductive structure by 3D printing technology is expected to be a new strategy for integrated and customized preparation of polymer-based electromagnetic shielding materials with low reflection and high absorption. Herein, we report an effective strategy to fabricate gradient-conductive transition-metal carbides/carbon nanotube/polyimide (gradient-conductive MXene/CNT/PI, GCMCP) aerogel frames with hierarchical porous structure via 3D printing technology. The integrated gradient-conductive structure from bottom to top is directly formed by continuous 3D printing of MXene/CNT/poly (amic acid) (MXene/CNT/PAA) composite inks with different CNT contents. In the GCMCP aerogel frames, the slightly conductive top layer of MCP aerogel serves as the EM absorption layer (impedance matching layer), while the highly conductive bottom layer of MCP aerogel as an EM reflection layer, forming an absorption-reflection-reabsorption interface. In addition, the hierarchical porous structure (lattice macrostructure and aerogel porous microstructure) of GCMCP aerogel frames extends the electromagnetic wave dissipation path by limiting the incident waves to enter the material in a specific direction and dissipates the electromagnetic wave by multiple reflections. As expected, the GCMCP aerogel frames

shows high EMI *SE* (68.2 dB) as well as low reflection coefficient (*R* = 0.23). The custom-designed GCMCP aerogel frames as electromagnetic shielding gasket is further demonstrated by a practical application in blocking power transmission. This work provides a novel strategy for designing EMI shielding materials with low EM wave reflection, which has a prosperous application potential in the high-end EMI shielding fields, such as the national defense industry and aerospace.

2 Experimental Section

2.1 Materials

Lithium fluoride (LiF, 99%) was purchased by Sigma-Aldrich Co., Ltd. Ti_3AlC_2 powder was obtained from Jilin 11 Technology Co., Ltd. 4,4'-diaminodiphenyl ether (ODA, 99%), pyromellitic dianhydride (PMDA), N, N-dimethylacetamide (DMAc), hydrochloric acid (HCl, 37%), and triethylamine (TEA) were all purchased from Sinopharm Chemical Reagent Co. Multiwalled carbon nanotubes (CNT, TNWDM-M8) were acquired from Chengdu Organic Chemicals Co. Ltd.

2.2 Preparation of MXene Sheets

MXene sheets with accordion-like structure were successfully synthesized through etching Ti_3AlC_2 powder in the LiF/HCl solution, as noted in reported work [28, 29]. Firstly, LiF (1 g) was added into HCl (20 mL, 9 mol L^{-1}) and stirred (500 r min^{-1}) at room temperature for 10 min. Subsequently, Ti_3AlC_2 powder was added into the above solution, and the mixed solution was continuously stirred for 24 h at 35 ℃. The multilayered MXene was washed with deionized water for 7–8 times, and centrifuged at 5,000 rpm for 5 min. Finally, the multilayer MXene dispersion was subjected to high-speed centrifugation at 10,000 rpm for 60 min and then freeze-drying to obtain the few-layered MXene powder.

2.3 Preparation of the MXene/CNT/PAA Composite Inks

The poly (amic acid) (PAA) salt precursors are prepared based on previous work [30–32]. 0.5 g PAA was first dispersed in 10 mL MXene suspension (50 mg mL^{-1}) and stirred for 6 h to obtain MXene/CNT/PAA-0 composite ink. Then, the CNT (0.25 g, 25 mg mL^{-1}) was added to the above MXene/PAA ink to obtain MXene/CNT/PAA-25 composite ink. Different conductive inks were obtained by changing CNT content. According to the different CNT contents (0, 25, 50 and 100 mg mL^{-1}), the composite inks were named MXene/CNT/PAA-0, MXene/CNT/PAA-25, MXene/CNT/PAA-50 and MXene/CNT/PAA-100, respectively (Table S1).

2.4 3D Printing Process and Fabrication of Gradient-Conductive MXene/CNT/Polyimide Aerogel Frames

The prepared MXene/CNT/PAA composite inks with different CNT content composite loaded into the separate syringes and extrusion-printed using a 3D printer (BP6601, China). Here, we designed geometric pattern with varies shapes by CAD software in advance, and then imported them into the printer. Firstly, we used the MXene/CNT/PAA-100 composite ink to print lattice structure as the bottom layer, then switch to MXene/CNT/PAA-25 composite ink to print lattice structure as the middle layer, and the top-layered lattice structure is printed with MXene/CNT/PAA-0 composite ink. Finally, the GCMCP-(0–25–100) aerogel frame could be obtained by freeze-drying for removing the ice crystal and thermal imidization at 300 °C in an argon atmosphere. We constructed three gradient-conductive structure, named GCMCP-(X_1-X_2-X_3), in which X_1, X_2 X_3 represent the CNT content in the top layer, middle layer and bottom layer of GCMCP aerogel frame, respectively (Table S2).

2.5 Characterizations

The morphologies of the GCMCP aerogel frame and multilayered MXene were investigated by scanning electron microscope (FESEM, JSM-7500F, Japan). The few-layered MXene sheets were characterized by transmission electron microscopy (TEM, JEM-2100F, Japan). The XRD spectra of MAX(Ti_3AlC_2) and MXene were characterized by X-ray diffraction (DX-2700BH, China). Fourier-transform infrared spectra (FTIR) were recorded with a Nicolet 6700 FTIR spectrophotometer (Bruker Spectrum Instruments, USA). The rheological properties of the MXene/CNT/PAA composite inks were measured by modular compact rheometer (MCR302, China), and the scanning range of shear rate was

of 0.01–100 s^{-1}. The mechanical properties were measured in the electronic universal testing machine (UTM2102, China) with a sensor of 100 N. The electrical conductivity was recorded by four-probe tester (MCP-T610, Mitsubishi Chemical). Conductivity of the gradient structure is calculated according to Eq. (1) [33]:

$$\sigma = \frac{l}{Rwd} \tag{1}$$

where σ is the conductivity; R is the resistance of sample; l, w and d are the thickness, width and distance between test electrodes, respectively. The resistance was measured by the resistance tester (2612B, Keithley, USA). The EMI shielding characteristics of aerogels were evaluated by the vector network analyzer (ZNB40, China) in X-band frequency range (8.2–12.4 GHz). The EMI shielding parameters are as follows: scattering parameters (S_{11} and S_{21}), reflection coefficient (R), transmission coefficient (T), absorption coefficient (A), total EMI shielding effectiveness (SE_T), electromagnetic waves reflection (SE_R), electromagnetic waves absorption (SE_A), and the calculation formula is as follows [15, 19]:

$$R = |S_{11}|^2 \tag{2}$$

$$T = |S_{21}|^2 \tag{3}$$

$$A = 1 - (R + T) \tag{4}$$

$$SE_T = 10 \log \left(\frac{1}{T} \right) \tag{5}$$

$$SE_R = 10 \log \left(\frac{1}{1 - R} \right) \tag{6}$$

$$SE_A = 10 \log \left(\frac{1 - R}{T} \right) \tag{7}$$

3 Results and Discussion

3.1 Fabrication of the GCMCP Aerogel Frames

The fabrication process of 3D printed gradient-conductive MXene/CNT/PI (GCMCP) aerogel frame is schematically exhibited in Fig. 1a. Briefly, a homogeneous MXene/CNT/PAA ink is obtained by dispersing the MXene, CNT and PAA in deionized water with magnetic stirring. Then, MXene/CNT/PAA inks with different CNT contents

are placed in the multiple feed system, and continuously deposited layer by layer on the plate through a 3D printer to prepare the gradient-conductive MXene/CNT/PAA gel frames. Afterward, with further freeze-drying for removing ice crystals and thermal imidization, a GCMCP aerogel frame with gradient-conductive and hierarchical porous structure is obtained. The successful thermal imidization of PAA into PI was verified by the FTIR spectra. As shown in Fig. S1a, new peaks located at 1720 cm^{-1} (C=O) and 1373 cm^{-1} (C-N) appear for MXene/CNT/PI, corresponding to the characteristic peaks of the imides in PI, indicating that the PAA is converted into PI [34, 35]. In addition, MXene exhibits excellent structural stability during thermal imidization (Fig. S1b). The average conductivity of MXene/CNT/PAA is 38.1 S cm^{-1}, which slightly increases to 40 S cm^{-1} after thermal imidization. The increase in conductivity is attributed to the removal of inserted water and other molecules during imidization, thus reducing the interlayer spacing of MXene nanosheets. The strategy achieves the accurate construction and integrated molding of gradient-conductive structure and imparts hierarchical porous structure (lattice macrostructure and aerogel porous microstructure) to GCMCP aerogel frame (Fig. 1b). In the GCMCP aerogel frame, the conductivity gradually increases from top to bottom, where the top layer serving as the absorbing layer (impedance match layer) and the bottom layer as the high reflective layer (impedance mismatch layer), forming an absorption-reflection-reabsorption interface [36]. Moreover, the middle layer acts as the transition layer that can enable GCMCP aerogel frame to reflect and dissipate electromagnetic waves through multi-interface reflection. In addition, the lattice structure of GCMCP aerogel frame extends the transmission path of electromagnetic waves and increases the multiple reflections inside aerogel pore walls, which greatly improves the EMI shielding performance [37, 38]. The free electrons of the transition-metal carbide/nitride backbone endow MXene with metallic conductivity, which can dissipate electromagnetic waves through ohmic losses [39]. Furthermore, MXene nanosheets with Ti elements can form partial dipoles with surface functional groups (=O, −F, −OH) in electric fields and the strong electronegativity of F elements can induce polarization [40, 41]. The large mismatch of the interface between MXene and PI also leads to high interfacial polarization, conferring excellent absorption properties to the GCMCP aerogel frame [42, 43]. Therefore, the GCMCP aerogel frame with gradient-conductive

structure can be further used to shield electromagnetic waves with low electromagnetic radiation pollution.

3.2 Formation and Morphology of GCMCP Aerogel Frames

The MXene/CNT/PAA inks with appropriate rheological properties are a prerequisite for 3D printing to accurately build gradient-conductive structure and hierarchical porous structure. The MXene sheets and CNT in the MXene/CNT/PAA inks serve as effective rheological modifiers by creating a stable structure through hydrogen bonding with PAA (Fig. 2a) [44, 45]. As shown by FTIR spectra in Fig. S2, the C=O peak of MXene/CNT/PAA shifts slightly from 1721 to 1719 cm^{-1}, mainly due to the hydrogen bonding interaction between the C=O group in the PAA and the carboxyl/hydroxyl group in the MXene/CNT [34]. The two-dimensional MXene sheets with high aspect ratio and a monolithic layer structure are prepared by etching the Ti$_3$AlC$_2$ phase with LiF/HCl solution followed by exfoliation (Fig. S3a-b). Moreover, the successful preparation of MXene sheets is evidenced by the XRD patterns, that (104) peak almost disappears and (002) peak is broadened, implying the successful elimination of Al after etching and expansion of interlayer spacing (Fig. S3c) [46]. In addition, one-dimensional CNTs are used as bridges to connect two-dimensional MXene sheets, thus constructing a continuous conductive network [47]. The viscosity variations of MXene/CNT/PAA inks with different CNT contents (0, 25, 50, and 100 mg mL^{-1}) are shown in Fig. 2b. The corresponding composite inks are named as MXene/CNT/PAA-0, MXene/CNT/PAA-25, MXene/CNT/PAA-50 and MXene/CNT/PAA-100, respectively (Table S1). All MXene/CNT/PAA inks show significant shear-thinning behaviors, which provides favorable conditions for continuous extrusion of inks. Furthermore, the storage modulus (G') of all MXene/CNT/PAA inks is higher than the loss modulus (G'') at low shear strain, showing the gel characteristics, which allows it self-supporting to maintain the printed structure (Fig. 2c) [45]. The stability of MXene/CNT/PAA inks with different CNT contents, further demonstrating good printability (Fig. S4). Therefore, the combination of continuous extrusion and self-supporting properties of MXene/CNT/PAA inks through 3D printing technology allows the integrated molding of high-precision GCMCP aerogel frames. As shown in Fig. 2d–e,

GCMCP aerogel with various macroscopic structures, including honeycomb, diamond, cylindrical lattice structure, exquisite butterfly and snowflake, indicating the excellent printability of MXene/CNT/PAA inks. The printed GCMCP aerogel frame can stand on the bamboo leaves, indicating its lightweight nature (Fig. 2f).

The typical GCMCP aerogel frame with gradient-conductive structure and hierarchical porous structure (Fig. 2i). The color of the GCMCP aerogel frame gradually increased from top to bottom with the increase of CNT content. In addition, each layer is well connected, attributed to the strong hydrogen bonding effect of PAA in the MXene/CNT/PAA composite inks (Fig. S5). The SEM image of GCMCP exhibits a uniform lattice structure with filament spacing of 400 μm (Fig. 2g). Furthermore, the filament exhibits a typical aerogel structure with pore sizes ranging from 10 to 30 μm depending on various CNT contents (Figs. 2k and S6), resulting in a hierarchical porous structure consisting of lattice macrostructure and aerogel porous microstructure for the GCMCP aerogel frames. Moreover, MXene sheets and CNTs are interconnected and uniformly distributed in PI matrix, forming a continuous and strong conductive network in aerogel (TEM image in Fig. 2l). In addition, the energy-dispersive spectroscopy (EDS) mapping images also display the existence and distribution of carbon (C), nitrogen (N), oxygen (O), fluorine (F) and titanium (Ti) elements on the pore wall, further proving the uniform distribution of MXene and CNTs in PI matrix (Fig. S7). Moreover, the aerogel frame exhibits improved mechanical strength with the addition of CNT (Fig. S8), which provides the basis for constructing EMI shielding materials with good mechanical performance [29].

3.3 EMI Shielding Performance of the MCP and GCMCP Aerogel Frames

To highlight the advantages of gradient-conductive structure in electromagnetic shielding, a non-gradient conductive MXene/CNT/PI-100 (MCP-100, 100 represents the content of CNT) aerogel frame is constructed for comparison (Fig. 3a). For the non-gradient conductive MCP-100 aerogel frame, the incident electromagnetic waves are easily reflected at the air-aerogel interface owing to high impedance mismatch, which inevitably brings the high secondary radiation pollution of electromagnetic waves. In contrast,
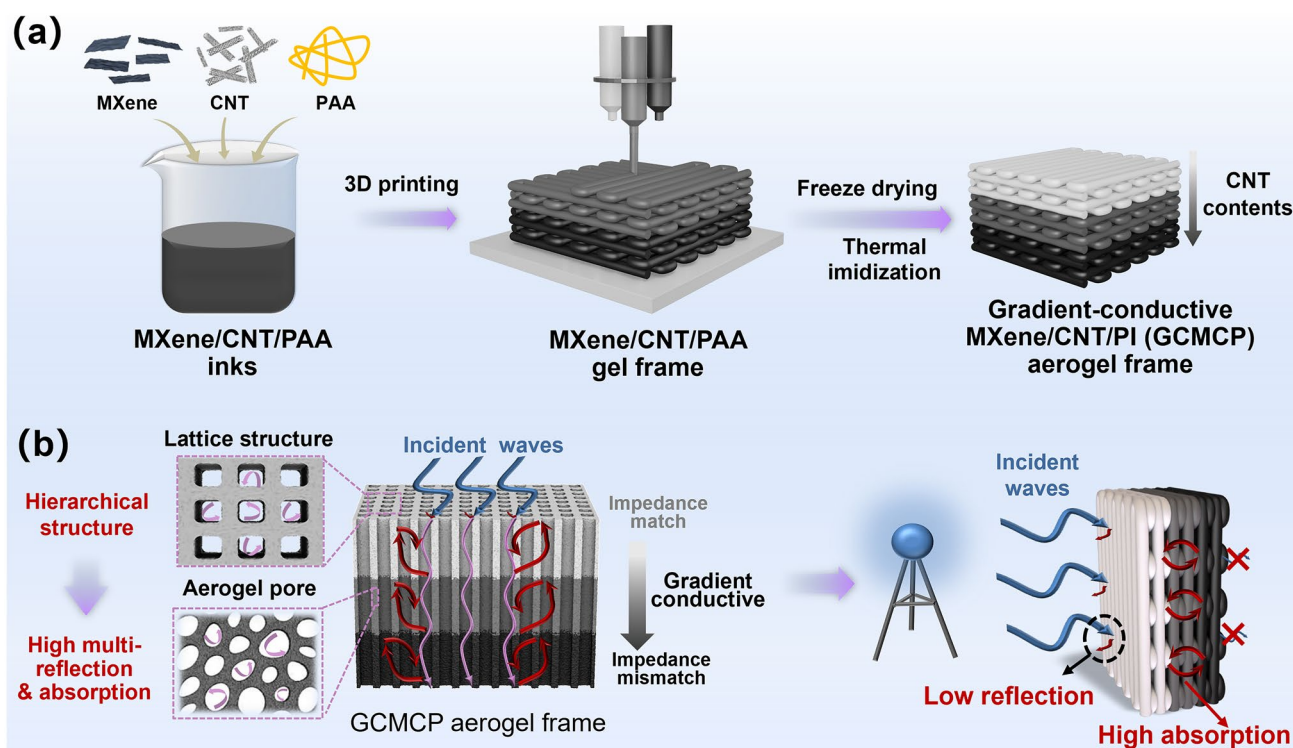
Fig. 1 (**a**) Schematic illustration of the fabrication process of the GCMCP aerogel frame. (**b**) Schematic diagram of EMI shielding mechanism of GCMCP aerogel frame and its application in the EMI shielding to reduce electromagnetic radiation pollution

the gradient-conductive GCMCP aerogel frame provides an impedance matching layer, so the incident wave can pass smoothly through the air-aerogel interface. And multi-interface reflections are generated between different conductive layers to continuously attenuate electromagnetic waves, which can reduce secondary radiation pollution of electromagnetic waves. In order to construct the gradient-conductive structure, the electrical conductivity and EMI shielding properties of each layer are adjusted by CNT contents. When the CNT contents of MCP-X (X = 0, 25, 50, 100; represents CNT contents) aerogel frame increase from 25 to 100 mg mL^{-1}, the conductivity increases from 17.3 to 41.0 S m^{-1} and the EMI SE increases from 36.6 to 49 dB (Fig. S9a). Furthermore, MCP aerogel frames show a negligible decrease in conductivity after storing in 50 ℃ and 95% relative humidity environment for 2 days (Fig. S9b), indicating its good stability due to the protection of polyimide that can effectively prevent MXene from oxidation [35]. The GCMCP-(X_1–X_2–X_3) aerogel frames with gradient-conductive structure are prepared by integrated and continuous 3D printing, in which X_1, X_2 X_3 represent the CNT content in the top layer (impedance match layer),

middle layer (transition layer) and bottom layer (impedance mismatch layer) (Table S2). The average EMI *SE* value at X band of GCMCP-(0–25–100) aerogel frame with gradient-conductive structure can reach 65.1 dB, which is higher than that of non-gradient conductive MCP-100 aerogel frame (EMI *SE* = 50 dB).

To further illustrate the EMI shielding mechanism of the GCMCP aerogel frames, the total EMI shielding effectiveness (SE_T), shielding effectiveness of the reflection (SE_R), and shielding effectiveness of the absorption (SE_A) are shown in Fig. 3c. Compared with MCP-100 aerogel frame (SE_R = 6.6 dB), GCMCP-(0–25–100) aerogel frame has lower SE_R (1.4 dB), which can be attributed to that the impedance matching layer in GCMCP-(0–25–100) aerogel frame can reduce the reflection of electromagnetic waves on the air-aerogel interface. In addition, the high SE_A (63.7 dB) of GCMCP-(0–25–100) aerogel frame is attributed to the absorption-reflection-reabsorption interface in the gradient-conductive structure aerogel frame. Furthermore, the CNT content in each layer is adjusted to maximize the EMI shielding and electromagnetic wave adsorption. When the CNT content of bottom layer decreased to 50 mg mL^{-1}, the
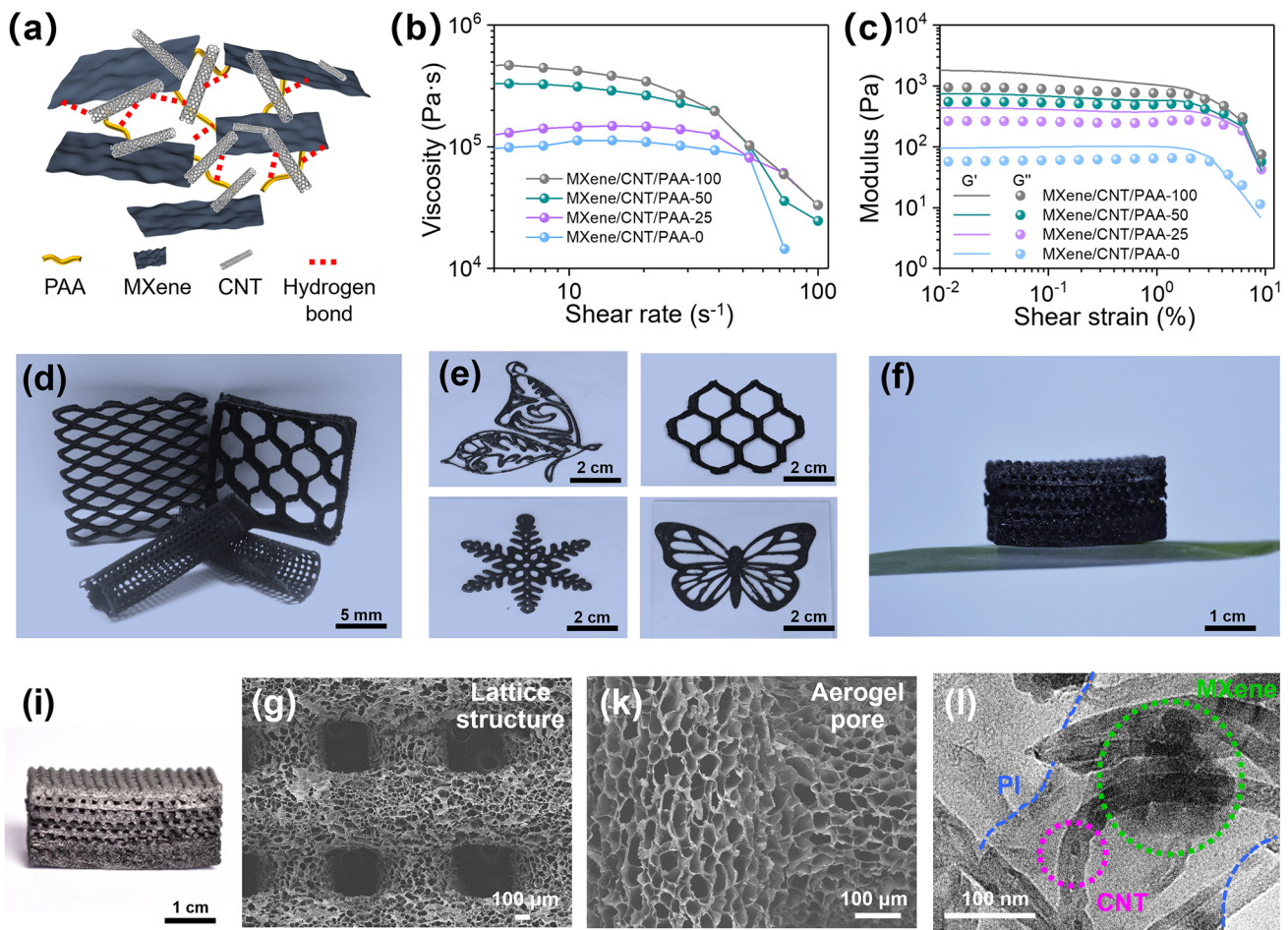
Fig. 2 Formation and morphology of GCMCP aerogel frames. (**a**) Illustration of the interaction of MXene, CNT and PAA in MXene/CNT/PAA inks. (**b**) Log–log plots of viscosity versus shear rate of MXene/CNT/PAA inks. (**c**) Log–log plots of the storage modulus (G') and loss modulus (G'') versus shear strain of MXene/CNT/PAA inks. (**d–e**) Optical images demonstrating the GCMCP aerogel frames with different macrostructures by 3D printing. (**f**) Optical image demonstrating the lightweight of GCMCP aerogel frame. (**i**) Optical image of GCMCP aerogel frames and corresponding (**g–k**) SEM images. (**l**) TEM images of GCMCP aerogel showing the morphology of aerogel pore walls

conductivity of GCMCP-(0–25–50) aerogel frame decreases to 23.6 S m^{-1}, and the corresponding EMI SE decreases to 47 dB (Figs. S10 and S11a), which is due to the low conductivity of bottom layer in the GCMCP-(0–25–50) aerogel frame resulting in weak electromagnetic losses. In addition, the conductivity of the GCMCP-(0–50–100) aerogel frame increased to 34.6 S cm^{-1} when the CNT content of the transition layer was increased to 50 mg mL^{-1}. The corresponding EMI SE increased to 78.5 dB and the SE$_R$ also increases to 7.5 dB (Fig. S11b). This high reflection owes to the large mismatch of conductivity in the interfaces between top layer and transition layer. Therefore, the reasonable gradient distribution of top layer (impedance match layer), middle layer (transition layer) and bottom layer (impedance mismatch layer) is of great significance to achieve high electromagnetic wave absorption and EMI shielding.

The EMI shielding performance of GCMCP aerogel frames with gradient-conductive structure is further investigated when electromagnetic waves incident from different incident directions. As shown in Fig. 3d–e, experiment "12" and experiment "21" represent the electromagnetic wave incident from the low conductive layer (MCP-0) and high conductive layer (MCP-100), respectively. When the electromagnetic waves are incident from the low conductive surface (MCP-0), the GCMCP-(0–25–100) aerogel frames have low average reflection coefficient (R, 0.27) and high average absorption coefficient (A, 0.73), which indicates that electromagnetic waves are dissipated by absorption (Figs. 3e
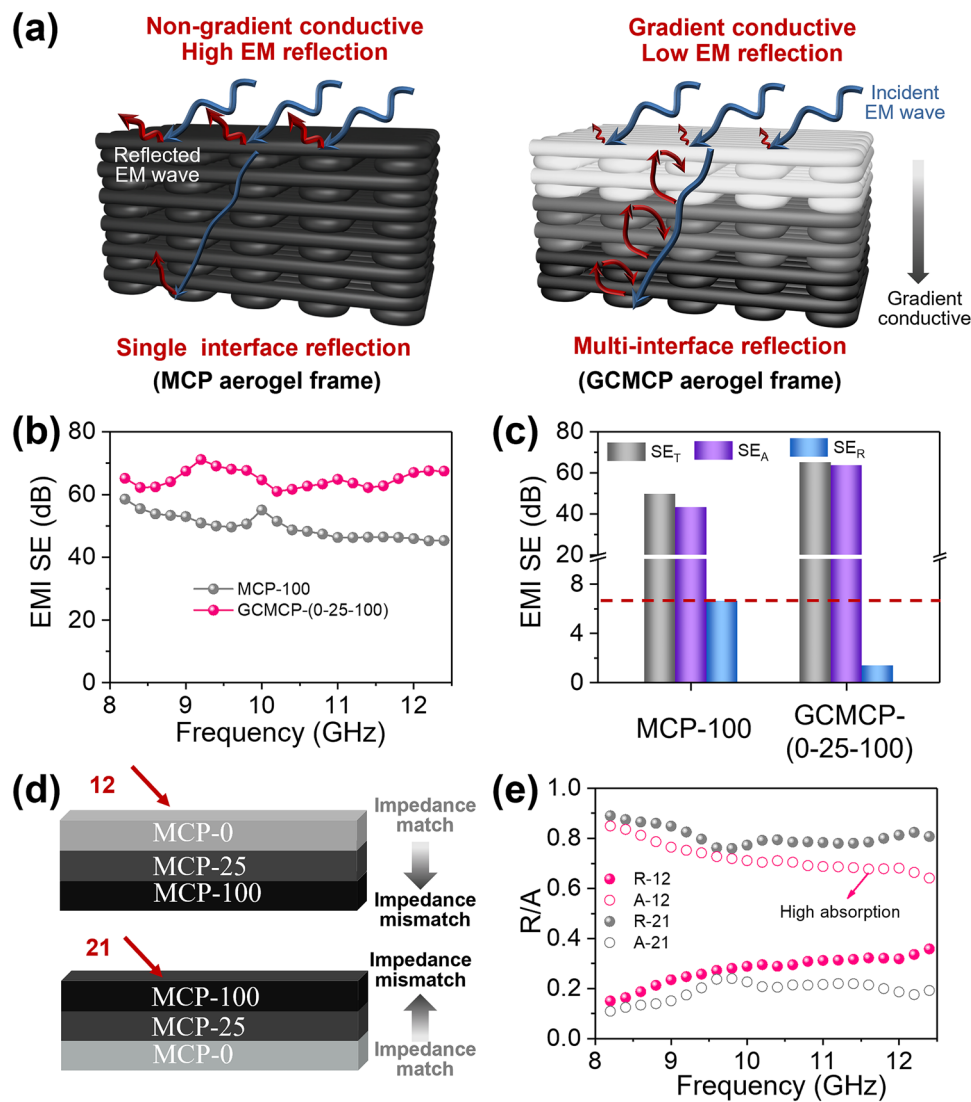
Fig. 3 Electromagnetic shielding performance of GCMCP aerogel with gradient-conductive structure at X band (thickness: about 5 mm). (**a**) Schematic representation of shielding mechanism of non-gradient conductive MCP aerogel frame and gradient-conductive GCMCP aerogel frame. (**b**) EMI shielding performances and (**c**) SE_T, SE_A, and SE_R value of MCP-100 aerogel and GCMCP-(0–25-100) aerogel frame. (**d**) Schematic diagram of electromagnetic wave incident from different directions. (**e**) Reflection/absorption coefficient of GCMCP-(0–25-100) aerogel frame at different incident directions

and S12). In contrast, when the electromagnetic waves are incident from the high conductive surface (MCP-100), the GCMCP-(0–25–100) aerogel frames have high average R (0.81) and low average A (0.19), demonstrating that electromagnetic waves are almost reflected into free space due to the impedance mismatch of air-aerogel interfaces, causing secondary EM wave contamination. Therefore, the incident electromagnetic waves from the low conductive layer can benefit the high adsorption of electromagnetic waves, which

highlights the merits of the unique asymmetric conductive structure.

3.4 EMI Shielding Performance of GCMCP Aerogel Frames with Different Lattice Size

Since the lattice structure of GCMCP aerogel frames could benefit to reduce the reflection and increase the absorption of electromagnetic waves, the effect of lattice size of
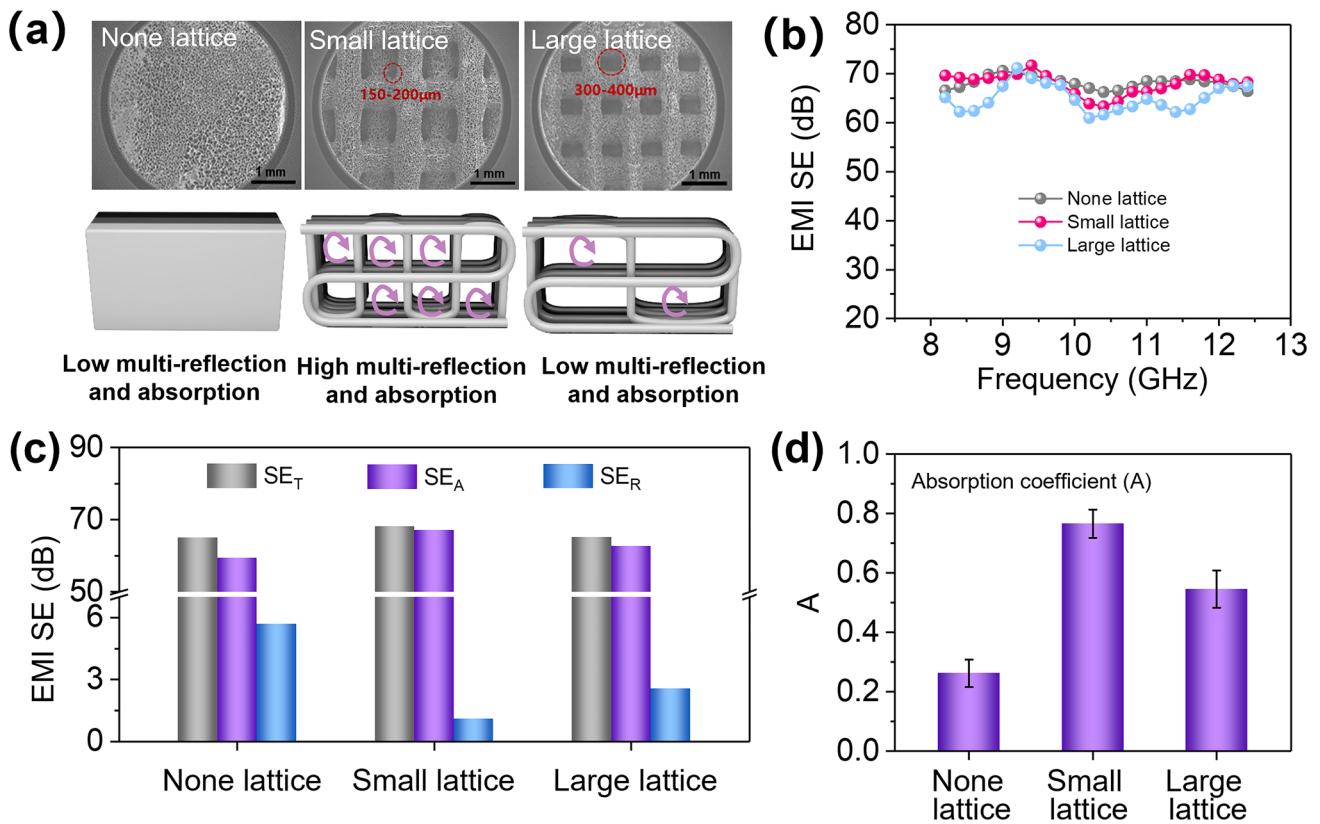
Fig. 4 Electromagnetic shielding performance of GCMCP aerogel frames with different lattice size, thickness: about 5 mm. (**a**) SEM images and EMI shielding mechanism of GCMCP aerogel frames with different lattice size. (**b**) EMI SE, (**c**) SE_T, SE_A and SE_R value and (**d**) absorption coefficient of none lattice, small lattice (150–200 μm) and large lattice (300–400 μm), respectively

aerogel frames on EMI shielding is further investigated. The design drawings and optical photographs of GCMCP aerogel frames with small and large lattice sizes are shown in Fig. S13. Figure 4a reveals the morphology and EMI shielding mechanism of GCMCP aerogel frames with different lattice size, where the small lattice size is 150–200 μm and the large lattice size is 300–400 μm. Compared with the non-lattice structure, the lattice structure introduced in GCMCP aerogel frame can lengthen the transmission path of electromagnetic waves inside the shielding material. At the same time, the hierarchical porous structure consisting of lattice structure and aerogel pores is more favorable to dissipate electromagnetic waves. It is worth noting that there is no significant change in EMI SE performance at X band as the lattice size increases (Fig. 4b). However, the SE_A is obviously improved for the small lattice structure ($SE_A = 67$ dB) as compared to the non-lattice ($SE_A = 59.3$ dB) and large

lattice ($SE_A = 62.6$ dB) structure, realizing high absorption by printed structure optimization (Fig. 4c). Subsequently, we further tested the A value to evaluate the effect of lattice structure on electromagnetic waves absorption capacity, which is shown in Fig. 4d. It can be clearly observed that lattice structure with small size shows obvious higher A value of 0.77, indicating that the GCMCP aerogel frames with smaller lattice size have stronger ability to absorb electromagnetic waves. Therefore, GCMCP aerogel frame with gradient-conductive structure and hierarchical porous structure results in low reflection and high absorption, which effectively reduces electromagnetic wave reflection.

3.5 Tunable EMI SE Performance of GCMCP Aerogel Frames with Different Thickness

The normalized electromagnetic shielding effectiveness is an important criterion to evaluate the EMI shielding
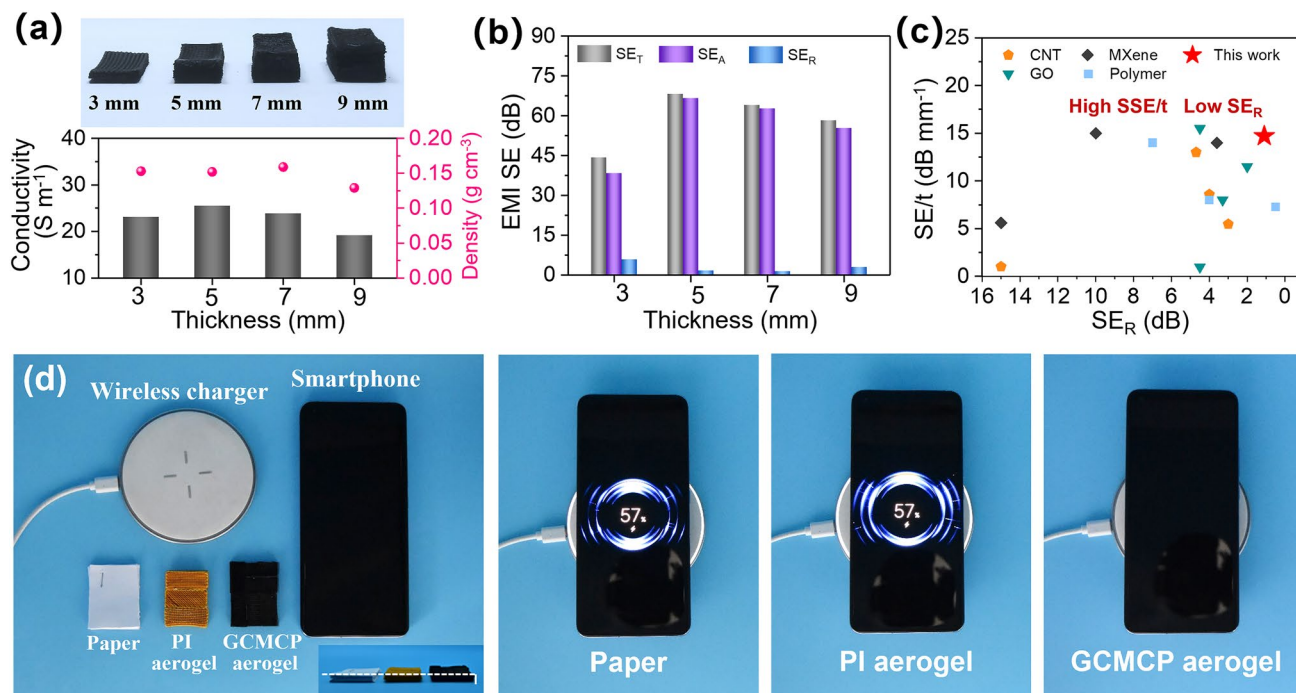
Fig. 5 Electromagnetic shielding performance of GCMCP aerogel frame with various thicknesses. (**a**) Digital photographs of GCMCP aerogel frame with 3, 5, 7 and 9 mm, and the conductivity and density as a function of thickness. (**b**) SE_T, SE_A and SE_R value of GCMCP aerogel frame with 3, 5, 7 and 9 mm, respectively. (**c**) Comparison of normalized EMI SE and SE_R with those of previously reported EMI shielding materials. (**d**) Demonstration of the EMI shielding ability of paper, PI aerogel frame and GCMCP aerogel frame for wireless charging

ability of porous materials, which includes three important parameters: the EMI *SE*, density and thickness. Here, we constructed GCMCP aerogel frames with thicknesses of 3, 5, 7 and 9 mm, respectively (Fig. 5a). The GCMCP aerogel frames have high conductivity (25.5 S m^{-1}) and low density (0.152 g cm^{-3}) at a thickness of 5 mm. Figure 5b displays the EMI *SE* performance of GCMCP aerogel frames with different thicknesses, and the GCMCP aerogel frame with thickness of 5 mm has the highest EMI *SE* of 68.2 dB and the lowest SE_R of 1.1 dB. However, the EMI *SE* of GCMCP aerogel frame decreases to 58.2 dB when the thickness increases to 9 mm. Theoretically, the impedance matching characteristic is usually measured by the Z_{in}-1 value, which can be calculated by the following equation [48–50]:

$$Z_{in} - 1 = \sqrt{\frac{\mu}{\varepsilon}} \tanh\left(j2\pi\sqrt{\mu\varepsilon}f\frac{d}{c}\right) - 1 \tag{8}$$

where c and f represent the light velocity (3×10^8 m s^{-1}) and EM frequency (8.2–12.4 GHz), ε and μ represent the permittivity and permeability, and d indicates the thickness of aerogel frame. When the thickness of aerogel frame increases from 3 to 9 mm, the thickness of the impedance

matching layer also increases from 1 to 3 mm, resulting in poor impedance matching and low EMI *SE*. We summarized the research progress of various EMI shielding materials in the literature, including MXene, CNT, polymer composite membranes/aerogels/frames [16, 51–62], and the results are shown in Fig. 5c and Table S3. The GCMCP aerogel frames with gradient-conductive structure and hierarchical porous structure exhibited high normalized EMI SE divided by thickness of 13.6 dB mm^{-1}, and ultra-low SE_R of 1.1 dB, which is better than previously reported. In addition, benefiting from the low density (0.152 g cm^{-3}) and high EMI shielding efficiency (68.2 dB) of GCMCP aerogel frames, the SSE (SE_T/density) is up to 448.7 dB cm^3 g^{-1}.

As a proof of concept for evaluating the EMI shielding of GCMCP aerogel frames in practical conditions, we placed paper, PI aerogel frame and GCMCP aerogel frame with the same thickness between smartphone and wireless charger, to observe the charging situation of the smartphone (Fig. 5d and Movie S1). Apparently, the smartphone can be easily charged on wireless charger covered with paper and PI aerogel frame, but cannot be charged on covering with GCMCP aerogel frames, indicating that GCMCP aerogel frames can act as EMI shielding gasket and effectively block wireless

power transmission process. Therefore, the 3D printing technology offers great flexibility for producing EMI shielding materials and devices with gradient-conductive structures for potential applications in electronic packaging.

4 Conclusions

In summary, a gradient-conductive and hierarchical porous GCMCP aerogel frame is designed by 3D printing technology as a high-performance EMI shielding material with ultra-low reflection coefficient. The GCMCP aerogel frame with controllable gradient-conductivity are obtained by adjusting the CNT contents of MXene/CNT/PAA ink, based on the continuous "bottom-up" 3D printing technology with the multi-feeding system. In the GCMCP aerogel frames, the slightly conductive top layer serves as the EM absorption layer, while the highly conductive bottom layer as an EM reflection layer, forming an absorption-reflection-reabsorption interface. Moreover, the hierarchical porous structure in the GCMCP aerogel frame dramatically improved the electromagnetic wave entering the material for multiple reflection loss. These unique structure designs enable the GCMCP aerogel framework with high EMI *SE* (68.2 dB) and ultra-low *R* (0.23), compared with traditional polymer composite membranes/aerogels/frames. The integrated gradient-conductive GCMCP aerogel frames represent a promising future research direction for developing advanced EMI shielding materials for microelectronics.

References

1. J. Liu, H.B. Zhang, R.H. Sun, Y.F. Liu, Z.S. Liu et al., Hydrophobic, flexible, and lightweight MXene foams for high-performance electromagnetic-interference shielding. Adv. Mater. **29**(38), 1702367 (2017). https://doi.org/10.1002/adma.201702367

2. J.Y. Zong, X.J. Zhou, Y.F. Hu, T.B. Yang, D.X. Yan et al., A wearable multifunctional fabric with excellent electromagnetic interference shielding and passive radiation heating performance. Compos. Part B Eng. **225**, 109299 (2021). https://doi.org/10.1016/j.compositesb.2021.109299

3. R. Baan, Y. Grosse, B. Lauby-Secretan, F. El Ghissassi, V. Bouvard et al., Carcinogenicity of radiofrequency electromagnetic fields. Lancet Oncol. **12**(7), 624–626 (2011). https://doi.org/10.1016/s1470-2045(11)70147-4

4. X.F. Liu, Y. Li, X. Sun, W.K. Tang, G. Deng et al., Off/on switchable smart electromagnetic interference shielding aerogel. Matter **4**(5), 1735–1747 (2021). https://doi.org/10.1016/j.matt.2021.02.022

5. H. Abbasi, M. Antunes, J.I. Velasco, Recent advances in carbon-based polymer nanocomposites for electromagnetic interference shielding. Prog. Mater. Sci. **103**, 319–373 (2019). https://doi.org/10.1016/j.pmatsci.2019.02.003

6. Y.L. Zhang, J.W. Gu, A perspective for developing polymer-based electromagnetic interference shielding composites. Nano-Micro Lett. **14**(1), 89 (2022). https://doi.org/10.1007/s40820-022-00843-3

7. N. Yousefi, X.Y. Sun, X.Y. Lin, X. Shen, J.J. Jia et al., Highly aligned graphene/polymer nanocomposites with excellent dielectric properties for high-performance electromagnetic interference shielding. Adv. Mater. **26**(31), 5480–5487 (2014). https://doi.org/10.1002/adma.201305293

8. D.X. Yan, H. Pang, B. Li, R. Vajtai, L. Xu et al., Structured reduced graphene oxide/polymer composites for ultra-efficient electromagnetic interference shielding. Adv. Funct. Mater. **25**(4), 559–566 (2015). https://doi.org/10.1002/adfm.201403809

9. M.L. Cheng, M.F. Ying, R.Z. Zhao, L.Z. Ji, H.X. Li et al., Transparent and flexible electromagnetic interference shielding materials by constructing sandwich AgNW@MXene/wood composites. ACS Nano **16**(10), 16996–17007 (2022). https://doi.org/10.1021/acsnano.2c07111

10. M. Wang, X.H. Tang, J.H. Cai, H. Wu, J.B. Shen et al., Construction, mechanism and prospective of conductive polymer composites with multiple interfaces for electromagnetic interference shielding: A review. Carbon **177**, 377–402 (2021). https://doi.org/10.1016/j.carbon.2021.02.047

11. L. Wang, Z.L. Ma, H. Qiu, Y.L. Zhang, Z. Yu et al., Significantly enhanced electromagnetic interference shielding performances of epoxy nanocomposites with long-range aligned lamellar structures. Nano-Micro Lett. **14**(1), 224 (2022). https://doi.org/10.1007/s40820-022-00949-8

12. Q.F. Guan, Z.M. Han, K.P. Yang, H.B. Yang, Z.C. Ling et al., Sustainable double-network structural materials for electromagnetic shielding. Nano Lett. **21**(6), 2532–2537 (2021). https://doi.org/10.1021/acs.nanolett.0c05081

13. Y.A. Chen, P. Potschke, J. Pionteck, B. Voit, H.S. Qi, Multifunctional cellulose/rGO/Fe$_3$O$_4$ composite aerogels for electromagnetic interference shielding. ACS Appl. Mater. Interfaces **12**(19), 22088–22098 (2020). https://doi.org/10.1021/acsami.9b23052

14. F. Pan, Y.P. Rao, D. Batalu, L. Cai, Y.Y. Dong et al., Macroscopic electromagnetic cooperative network-enhanced MXene/Ni chains aerogel-based microwave absorber with ultra-low matching thickness. Nano-Micro Lett. **14**(1), 140 (2022). https://doi.org/10.1007/s40820-022-00869-7

15. S. Zhao, H.B. Zhang, J.Q. Luo, Q.W. Wang, B. Xu et al., Highly electrically conductive three-dimensional Ti$_3$C$_2$T$_x$ MXene/reduced graphene oxide hybrid aerogels with excellent electromagnetic interference shielding performances. ACS Nano **12**(11), 11193–11202 (2018). https://doi.org/10.1021/acsnano.8b05739

16. Z.H. Zeng, T.T. Wu, D.X. Han, Q. Ren, G. Siqueira et al., Ultralight, flexible, and biomimetic nanocellulose/silver nanowire aerogels for electromagnetic interference shielding. ACS Nano **14**(3), 2927–2938 (2020). https://doi.org/10.1021/acsnano.9b07452

17. Y.D. Xu, Y.Q. Yang, D.X. Yan, H.J. Duan, G.Z. Zhao et al., Gradient structure design of flexible waterborne polyurethane conductive films for ultraefficient electromagnetic shielding with low reflection characteristic. ACS Appl. Mater. Interfaces **10**(22), 19143–19152 (2018). https://doi.org/10.1021/acsami.8b05129

18. Y.Q. Hu, C. Hou, Y.X. Shi, J.M. Wu, D. Yang et al., Freestanding Fe$_3$O$_4$/Ti$_3$C$_2$T$_x$ MXene/polyurethane composite film with efficient electromagnetic shielding and ultra-stretchable performance. Nanotechnology **33**(16), 165603 (2022). https://doi.org/10.1088/1361-6528/ac4878

19. B. Xue, Y. Li, Z.L. Cheng, S.D. Yang, L. Xie et al., Directional electromagnetic interference shielding based on step-wise asymmetric conductive networks. Nano-Micro Lett. **14**(1), 16 (2021). https://doi.org/10.1007/s40820-021-00743-y

20. Z.M. Lei, D.K. Tian, X.B. Liu, J.H. Wei, K. Rajavel et al., Electrically conductive gradient structure design of thermoplastic polyurethane composite foams for efficient electromagnetic interference shielding and ultra-low microwave reflectivity. Chem. Eng. J. **424**, 130365 (2021). https://doi.org/10.1016/j.cej.2021.130365

21. J.M. Yang, X. Liao, G. Wang, J. Chen, F.M. Guo et al., Gradient structure design of lightweight and flexible silicone rubber nanocomposite foam for efficient electromagnetic interference shielding. Chem. Eng. J. **390**, 124589 (2020). https://doi.org/10.1016/j.cej.2020.124589

22. A. Bandyopadhyay, B. Heer, Additive manufacturing of multi-material structures. Mater. Sci. Eng. R Rep. **129**, 1–16 (2018). https://doi.org/10.1016/j.mser.2018.04.001

23. L.A.E. Müller, T. Zimmermann, G. Nyström, I. Burgert, G. Siqueira, Mechanical properties tailoring of 3D printed photoresponsive nanocellulose composites. Adv. Funct. Mater. **30**(35), 2002914 (2020). https://doi.org/10.1002/adfm.202002914

24. R.S. Ambekar, B. Kushwaha, P. Sharma, F. Bosia, M. Fraldi et al., Topologically engineered 3D printed architectures with superior mechanical strength. Mater. Today **48**, 72–94 (2021). https://doi.org/10.1016/j.mattod.2021.03.014

25. J.Z. Feng, B.L. Su, H.S. Xia, S.Y. Zhao, C. Gao et al., Printed aerogels: Chemistry, processing, and applications. Chem. Soc. Rev. **50**(6), 3842–3888 (2021). https://doi.org/10.1039/c9cs00757a

26. W. Zong, N.B. Chui, Z.H. Tian, Y.T. Li, C. Yang et al., Ultrafine MOP nanoparticle splotched nitrogen-doped carbon nanosheets enabling high-performance 3D-printed potassium-ion hybrid capacitors. Adv. Sci. **8**(7), 2004142 (2021). https://doi.org/10.1002/advs.202004142

27. Y. Kwon, S.E. Seo, J. Lee, S. Berezvai, J. Read de Alaniz et al., 3D-printed polymer foams maintain stiffness and energy dissipation under repeated loading. Compos. Commun. (2022). https://doi.org/10.1016/j.coco.2022.101453

28. L. Pu, Y.P. Liu, L. Li, C. Zhang, P.M. Ma et al., Polyimide nanofiber-reinforced Ti$_3$C$_2$T$_x$ aerogel with "lamella-pillar" microporosity for high-performance piezoresistive strain sensing and electromagnetic wave absorption. ACS Appl. Mater. Interfaces **13**(39), 47134–47146 (2021). https://doi.org/10.1021/acsami.1c13863

29. C.H. Lin, S.H. Luo, F.C. Meng, B. Xu, T. Long et al., MXene/air-laid paper composite sensors for both tensile and torsional deformations detection. Compos. Commun. **25**, 100768 (2021). https://doi.org/10.1016/j.coco.2021.100768

30. T.T. Xue, C.Y. Zhu, X.L. Feng, Q. Wali, W. Fan et al., Polyimide aerogel fibers with controllable porous microstructure for super-thermal insulation under extreme environments. Adv. Fiber Mater. **4**(5), 1118–1128 (2022). https://doi.org/10.1007/s42765-022-00145-8

31. J. Tian, Y. Yang, T.T. Xue, G.J. Chao, W. Fan et al., Highly flexible and compressible polyimide/silica aerogels with integrated double network for thermal insulation and fire-retardancy. J. Mater. Sci. Technol. **105**, 194–202 (2022). https://doi.org/10.1016/j.jmst.2021.07.030

32. C.Y. Zhu, F. Yang, T.T. Xue, Q. Wali, W. Fan et al., Metal-organic framework decorated polyimide nanofiber aerogels for efficient high-temperature particulate matter removal. Sep. Purif. Technol. **300**, 121881 (2022). https://doi.org/10.1016/j.seppur.2022.121881

33. H.C. Lu, Z.H. Xia, X.J. Zheng, Q.Y. Mi, J.M. Zhang et al., Patternable cellulose/MWCNT laminated nanocomposites with anisotropic thermal and electrical conductivity. Compos. Commun. **26**, 100786 (2021). https://doi.org/10.1016/j.coco.2021.100786

34. D. Wang, Y.D. Peng, J.C. Dong, L. Pu, K.Q. Chang et al., Hierarchically porous polyimide aerogel fibers based on the confinement of Ti$_3$C$_2$T$_x$ flakes for thermal insulation and fire retardancy. Compos. Commun. **37**, 101429 (2023). https://doi.org/10.1016/j.coco.2022.101429

35. J. Liu, H.B. Zhang, X. Xie, R. Yang, Z. Liu et al., Multifunctional, superelastic, and lightweight MXene/polyimide aerogels. Small **14**(45), e1802479 (2018). https://doi.org/10.1002/smll.201802479

36. L. Ma, M. Hamidinejad, B. Zhao, C.Y. Liang, C.B. Park, Layered foam/film polymer nanocomposites with highly efficient EMI shielding properties and ultralow reflection. Nano-Micro Lett. **14**(1), 19 (2021). https://doi.org/10.1007/s40820-021-00759-4

37. Z.X. Xie, Y.F. Cai, Z.J. Wei, Y.H. Zhan, Y.Y. Meng et al., Robust and self-healing polydimethylsiloxane/carbon nanotube foams for electromagnetic interference shielding and thermal insulation. Compos. Commun. **35**, 101323 (2022). https://doi.org/10.1016/j.coco.2022.101323

38. Z.B. Jiao, W.J. Huyan, F. Yang, J.R. Yao, R.Y. Tan et al., Achieving ultra-wideband and elevated temperature electromagnetic wave absorption via constructing lightweight porous rigid structure. Nano-Micro Lett. **14**(1), 173 (2022). https://doi.org/10.1007/s40820-022-00904-7

39. Q.Y. Li, M.L. Liu, B.C. Zhong, W.Q. Zhang, Z.X. Jia et al., Tetramethylammonium hydroxide modified MXene as a functional nanofiller for electrical and thermal conductive rubber composites. Compos. Commun. **34**, 101249 (2022). https://doi.org/10.1016/j.coco.2022.101249

40. T.Z. Zhou, Y.Z. Yu, B. He, Z. Wang, T. Xiong et al., Ultracompact MXene fibers by continuous and controllable synergy of interfacial interactions and thermal drawing-induced stresses. Nat. Commun. **13**(1), 4564 (2022). https://doi.org/10.1038/s41467-022-32361-6

41. F. Shahzad, M. Alhabeb, C.B. Hatter, B. Anasori, S. Man Hong et al., Electromagnetic interference shielding with 2D transition metal carbides (MXenes). Science **353**(6304), 1137–1140 (2016). https://doi.org/10.1126/science.aag2421

42. Z.H. Zeng, N. Wu, J.J. Wei, Y.F. Yang, T.T. Wu et al., Porous and ultra-flexible crosslinked MXene/polyimide composites for multifunctional electromagnetic shielding. Nano-Micro Lett. **14**(1), 59 (2022). https://doi.org/10.1007/s40820-022-00800-0

43. X.Q. Yang, Y.F. Zhang, J.M. Luo, R. Tusiime, C.Z. Lu et al., Fe$_3$O$_4$ uniformly decorated reduced graphene oxide aerogel for epoxy nanocomposites with high emi shielding performance. Compos. Commun. **36**, 101391 (2022). https://doi.org/10.1016/j.coco.2022.101391

44. H. Liu, X.Y. Chen, Y.J. Zheng, D.B. Zhang, Y. Zhao et al., Lightweight, superelastic, and hydrophobic polyimide nanofiber /MXene composite aerogel for wearable piezoresistive sensor and oil/water separation applications. Adv. Funct. Mater. **31**(13), 2008006 (2021). https://doi.org/10.1002/adfm.202008006

45. Y. Yang, W. Fan, S.J. Yuan, J. Tian, G.J. Chao et al., A 3D-printed integrated MXene-based evaporator with a vertical array structure for salt-resistant solar desalination. J. Mater. Chem. A **9**(42), 23968–23976 (2021). https://doi.org/10.1039/d1ta07225k

46. J.J. Liu, W.J. Yang, Y. Xu, A.C.Y. Yuen, T.B.Y. Chen et al., MXene-based films via scalable fabrication with improved mechanical and antioxidant properties for electromagnetic interference shielding. Compos. Commun. **31**, 101112 (2022). https://doi.org/10.1016/j.coco.2022.101112

47. T.Y. Zhu, Q.C. Feng, K.N. Wan, C. Zhang, B. Li et al., Articular cartilage-inspired 3D superelastic and fatigue-resistant spongy conductors against harsh environments. Sci. China Mater. (2022). https://doi.org/10.1007/s40843-022-2262-7

48. Z.M. Deng, P.P. Tang, X.Y. Wu, H.B. Zhang, Z.Z. Yu, Superelastic, ultralight, and conductive Ti$_3$C$_2$T$_x$ MXene/acidified carbon nanotube anisotropic aerogels for electromagnetic interference shielding. ACS Appl. Mater. Interfaces **13**(17), 20539–20547 (2021). https://doi.org/10.1021/acsami.1c02059

49. X.L. Li, X.W. Yin, H.L. Xu, M.K. Han, M.H. Li et al., Ultralight mxene-coated, interconnected sicnws three-dimensional lamellar foams for efficient microwave absorption in the x-band. ACS Appl. Mater. Interfaces **10**(40), 34524–34533 (2018). https://doi.org/10.1021/acsami.8b13658

50. K.S. Cole, R.H. Cole, Dispersion and absorption in dielectrics i alternating current characteristics. J. Chem. Phys. **9**(4), 341–351 (1941). https://doi.org/10.1063/1.1750906

51. Y.M. Huangfu, K.P. Ruan, H. Qiu, Y.J. Lu, C.B. Liang et al., Fabrication and investigation on the PANi/MWCNT/thermally annealed graphene aerogel/epoxy electromagnetic interference shielding nanocomposites. Compos. Part A Appl. Sci. Manuf. **121**, 265–272 (2019). https://doi.org/10.1016/j.compositesa.2019.03.041

52. Z.H. Zeng, H. Jin, M.J. Chen, W.W. Li, L.C. Zhou et al., Lightweight and anisotropic porous MWCNT/WPU composites for ultrahig performance electromagnetic interference shielding. Adv. Funct. Mater. **26**(2), 303–310 (2016). https://doi.org/10.1002/adfm.201503579

53. X.Y. Pei, G.D. Liu, R.Q. Shao, R.R. Yu, R.X. Chen et al., 3D-printing carbon nanotubes/Ti3C2Tx/chitosan composites with different arrangement structures based on ball milling for emi shielding. J. Appl. Polym. Sci. **139**(45), e53125 (2022). https://doi.org/10.1002/app.53125

54. B. Shen, Y. Li, W.T. Zhai, W.G. Zheng, Compressible graphene-coated polymer foams with ultralow density for adjustable electromagnetic interference (EMI) shielding. ACS Appl. Mater. Interfaces **8**(12), 8050–8057 (2016). https://doi.org/10.1021/acsami.5b11715

55. Y.J. Wan, P.L. Zhu, S.H. Yu, R. Sun, C.P. Wong et al., Ultralight, super-elastic and volume-preserving cellulose fiber/graphene aerogel for high-performance electromagnetic

interference shielding. Carbon **115**, 629–639 (2017). https://doi.org/10.1016/j.carbon.2017.01.054

56. Z.M. Fan, D.L. Wang, Y. Yuan, Y.S. Wang, Z.J. Cheng et al., A lightweight and conductive MXene/graphene hybrid foam for superior electromagnetic interference shielding. Chem. Eng. J. **381**, 122696 (2020). https://doi.org/10.1016/j.cej.2019.122696

57. B. Shen, W.T. Zhai, M.M. Tao, J.Q. Ling, W.G. Zheng, Lightweight, multifunctional polyetherimide/graphene@Fe$_3$O$_4$ composite foams for shielding of electromagnetic pollution. ACS Appl. Mater. Interfaces **5**(21), 11383–11391 (2013). https://doi.org/10.1021/am4036527

58. Y.Y. Wang, W.J. Sun, D.X. Yan, K. Dai, Z.M. Li, Ultralight carbon nanotube/graphene/polyimide foam with heterogeneous interfaces for efficient electromagnetic interference shielding and electromagnetic wave absorption. Carbon **176**, 118–125 (2021). https://doi.org/10.1016/j.carbon.2020.12.028

59. Z. Yu, T.W. Dai, S.W. Yuan, H.W. Zou, P.B. Liu, Electromagnetic interference shielding performance of anisotropic polyimide/graphene composite aerogels. ACS Appl. Mater. Interfaces **12**(27), 30990–31001 (2020). https://doi.org/10.1021/acsami.0c07122

60. X.H. Li, X.F. Li, K.N. Liao, P. Min, T. Liu et al., Thermally annealed anisotropic graphene aerogels and their electrically conductive epoxy composites with excellent electromagnetic interference shielding efficiencies. ACS Appl. Mater. Interfaces **8**(48), 33230–33239 (2016). https://doi.org/10.1021/acsami.6b12295

61. Z.H. Zeng, C.X. Wang, Y.F. Zhang, P.Y. Wang, S.I. Seyed Shahabadi et al., Ultralight and highly elastic graphene/lignin-derived carbon nanocomposite aerogels with ultrahigh electromagnetic interference shielding performance. ACS Appl. Mater. Interfaces **10**(9), 8205–8213 (2018). https://doi.org/10.1021/acsami.7b19427

62. B.H. Xia, X.H. Zhang, J. Jiang, Y. Wang, T. Li et al., Facile preparation of high strength, lightweight and thermal insulation polyetherimide/Ti$_3$C$_2$T$_x$ MXenes/Ag nanoparticles composite foams for electromagnetic interference shielding. Compos. Commun. **29**, 101028 (2022). https://doi.org/10.1016/j.coco.2021.101028